Separation and Purification Technology 328 (2024) 124993

Contents lists available at ScienceDirect

Separation and Purification Technology

journal homepage: www.elsevier.com/locate/seppur

Cobalt-doped cerium dioxide enhances interfacial synergistic catalysis for boosting the oxidation of toluene

Youcai Zhu [a,b], Caiting Li [a,*], Xuan Liu [a], Ying Zhang [a], Kuang Yang [a], Le Huang [a], Jungang Zhao [a], Ziang Zhang [a]

[a] College of Environmental Science and Engineering, Key Laboratory of Environmental Biology and Pollution Control (Ministry of Education), Hunan University, Changsha 410082, PR China

[b] Shandong Key Laboratory of Environmental Processes and Health, School of Environmental Science and Engineering, Shandong University, Qingdao 266237, PR China

ARTICLE INFO

Keywords:
Toluene
$CoCeO_x$ nanoparticles
Synergistic effect
Lower temperature
Catalytic oxidation

ABSTRACT

The $CoCeO_x$ nanoparticles ($CoCeO_x$-NP) with different Co/Ce molar ratios were successfully prepared and applied to toluene oxidation. Appropriate Co-doped CeO_2 significantly enhanced the interfacial synergistic catalysis to boost toluene oxidation. $CoCeO_x$-2-NP exhibited the highest toluene conversion activity (T_{50} = 203 °C, T_{90} = 209 °C) and CO_2 selectivity under the high weight hourly space velocity (WHSV). Various characterizations were performed to comprehensively analyze the relationship between the structure and performance of the catalysts. The high O_β/O_{tot}, good oxygen mobility, and the synergistic effects between cobalt and cerium showed excellent performance for toluene oxidation at lower temperatures. Besides, the $CoCeO_x$-2-NP catalysts exhibited good stability and reusability, making them potential for practical applications in toluene oxidation. Notably, the XPS, DFT, and in situ DRIFTS further investigated the pathway of toluene oxidation, which lays a foundation for an in-depth understanding of the oxidation behavior of toluene and the subsequent development of efficient catalytic materials.

1. Introduction

As a major air pollutant, volatile organic compounds (VOCs) are widely derived from industrial production, transport, and human activities [1]. Most VOCs are the critical precursors of $PM_{2.5}$ and photochemical smog, significantly contributing to environmental problems [1]. More seriously, VOCs emissions threaten the human living environment and health [2].

As a typical representative of VOCs, toluene has relatively stable properties and usually requires catalytic degradation at higher temperatures. Conventional control technologies such as adsorption, absorption, and biological degradation treatment make it difficult to effectively eliminate toluene in exhaust gas under energy-saving conditions [3–5]. As an economical and practical technology, the advantages of catalytic oxidation are particularly outstanding in treating low and medium VOCs concentrations [6,7]. Catalysts as the core of VOCs catalytic oxidation technology and their performance is widely affected by the composition and preparation method [8]. Generally, the performance of noble metal catalysts is better than transition metal catalysts at low temperatures [9]. However, the drawbacks of high prices and poor halogen resistance limit their widespread application. Meanwhile, transition metal catalysts have many significant advantages, such as low cost, good halogen resistance, thermal stability, etc [10,11]. Therefore, developing transition metal catalysts with high catalytic activity is desirable to replace noble metal catalysts for aromatic VOCs degradation at lower temperatures.

Great efforts have been made to enhance the catalytic performance of transition metal catalysts. One strategy is to synthesize the catalysts with a particular morphology (such as nanoparticles, nanorods, three-dimensional ordered structure, etc.) to expose more active reaction surfaces or increase the dispersion of active components. In fact, exposing different crystal surfaces is the essence of controlling the different morphologies of catalytic materials [12,13]. Another strategy is to create more oxygen vacancies on the surface of the catalyst. The common method is metal element doping, that is, adding one or more elements to the crystal structure of another element to generate more

* Corresponding author at: College of Environmental Science and Engineering, Key Laboratory of Environmental Biology and Pollution Control (Ministry of Education), Hunan University, Changsha 410082, PR China.
E-mail address: ctli@hnu.edu.cn (C. Li).

https://doi.org/10.1016/j.seppur.2023.124993
Received 28 June 2023; Received in revised form 24 August 2023; Accepted 30 August 2023
Available online 4 September 2023

surface defect sites to increase the active site required for catalytic oxidation [14,15].

Among the transition metal oxides, cerium dioxide (CeO_2) has good oxygen storage capacity and abundant surface oxygen species [16–18]. However, the low-temperature catalytic performance of cerium oxide cannot meet practical application requirements. Therefore, using a simple doping strategy to modify CeO_2 can cause lattice defects and generate more oxygen vacancies, which is expected to improve the catalytic performance of the catalyst for VOCs at low temperatures [19,20]. Among transition metals, cobalt oxide (CoO_x) is widely used in catalytic materials due to its low Co-O bond energy and high molecular oxygen activation ability [21]. Meanwhile, the atomic radius of cobalt (0.65 Å) is smaller than that of cerium (0.87 Å), it is easy to enter the crystal lattice of CeO_2 during preparation, causing lattice defects [22]. Besides, the synergistic effect between cobalt and cerium can be fully utilized [23].

In this work, toluene was selected as the target pollutant, the metal modification and morphology control were combined by a hard-template method, and the $CoCeO_x$ nanocatalyst was synthesized for toluene oxidation. Different characterizations systematically studied the synergistic effect between the Co_3O_4 and CeO_2 on toluene oxidation and the structure–activity relationships of $CoCeO_x$-NP catalysts. Besides, the performance parameters of the catalysts, such as thermal stability, water resistance, and recycling, were investigated. Finally, the intermediates of toluene oxidation on $CoCeO_x$-NP catalyst have been studied by DFT and in situ DRIFTS to assist in exploring the reaction path and mechanism.

2. Experimental

2.1. Catalyst preparation

All chemicals are analytical reagents (AR). The detailed information is listed in the Supplementary Material.

The polymethyl methacrylate (PMMA) microspheres (~200 nm) were synthesized as a template, and the detailed preparation process was described elsewhere [24,25].

The $CoCeO_x$ materials were synthesized through the hard-templating method. A certain amount of $Co(NO_3)_2{\cdot}6H_2O$ and $Ce(NO_3)_3{\cdot}6H_2O$ (mole ratio of Co/Ce = 0.5, 1, and 2) were dissolved in 20.0 mL mixed solution of methanol and ethylene glycol (volumetric ratio = 3:1). Besides, a certain amount of chelating agent (citric acid) was added and stirred for 3 h until a transparent mixed solution was obtained. Then, 5.0 g of PMMA was impregnated in the hybrid solution for 6 h and removed the excess solution by vacuum filtration. The obtained solids were dried at 30 °C for 48 h, then heated at 300 °C for 2 h in pure N_2. Finally, the solids were calcinated at 500 °C for 3 h in the air. The obtained samples with different Co/Ce were denoted as $CoCeO_x$-0.5-NP, $CoCeO_x$-1-NP, and $CoCeO_x$-2-NP. For comparison, Co_3O_4-NP and CeO_2-NP were also synthesized in the same method as above.

2.2. Catalyst characterizations

The various characterizations, such as X-ray diffraction (XRD), scanning electron microscopes (SEM), high-resolution field emission transmission electron microscopy (HRTEM), N_2 adsorption–desorption isotherm, H_2 temperature programmed reduction (H_2-TPR), O_2 temperature programmed desorption (O_2-TPD), Electron paramagnetic resonance (EPR), Raman spectroscopy (Raman), X-ray photoelectron spectroscopy (XPS), Fourier transform infrared spectrometer (FTIR), in situ diffuse reflectance infrared Fourier transform spectroscopy (in situ DRIFTS), and density function theory (DFT) calculation are described in detail in the Supplementary Material.

2.3. Catalytic activity test

The toluene catalytic oxidation performance of the samples was conducted in a fixed-bed reactor (Figure S1). 0.1 g catalysts were put into a quartz tubular microreactor (Φ = 6 nm). The total flow rate was 100 mL/min (including 1000 ppm toluene, 21 vol% O_2, and the balance N_2,) and the corresponding WHSV was 60 000 $mL{\cdot}h^{-1}{\cdot}g^{-1}$. The mass flow controllers precisely controlled the simulated flue gas. The reaction temperatures (160–320 °C) were precisely controlled by the digital temperature controller. The toluene vapor was generated by an N_2 bubbler in the ice-water bath, and its concentration was detected by gas chromatography equipped with a flame ionization detector (FID) (GC-2014C, Shimadzu, Japan). The intermediate species in the reaction process were detected by Gas Chromatography-Mass Spectrometer (GC–MS) (7890A-5975C, Agilent, USA). The efficiency of toluene (C_7H_8) conversion was calculated as follows:

$$C_7H_8\ \ conversion\ \ (\%) = \frac{C_7H_{8_{in}} - C_7H_{8_{out}}}{C_7H_{8_{in}}} \times 100\% \quad (1)$$

$$CO_2\ \ selectivity\ \ (\%) = \frac{CO_{2_{out}}}{7 \times (C_7H_{8_{in}} - C_7H_{8_{out}})} \times 100\% \quad (2)$$

where C_7H_{8in} and C_7H_{8out} are represent the toluene concentrations at the inlet and outlet of the fixed-bed reactor, respectively (ppm). T_{50} and T_{90} are usually used to evaluate the catalytic efficiency of the catalyst for toluene, representing the corresponding temperature when toluene conversion efficiency reaches 50% and 90%. Besides, CO_{2out} represents the CO_2 concentration (ppm) of the outlet of the reactor.

3. Results and discussion

3.1. The synergistic effects on catalytic oxidation performance of toluene

The relationship between temperature and Co/Ce on toluene conversion efficiency is presented in Fig. 1(A). The toluene conversion efficiency of samples increased with the temperature rise (160–320 °C) and presented a typical S-shaped curve, indicating that higher temperature is more conducive to toluene oxidation. The T_{50} of Co_3O_4-NP, CeO_2-NP, $CoCeO_x$-0.5-NP, $CoCeO_x$-1-NP, and $CoCeO_x$-2-NP catalysts is 272 °C, 255 °C, 245 °C, 228 °C, and 203 °C, respectively. The corresponding T_{90} for Co_3O_4-NP, $CoCeO_x$-0.5-NP, $CoCeO_x$-1-NP, and $CoCeO_x$-2-NP catalysts is 279 °C, 259 °C, 246 °C, and 209 °C, respectively (listed in Table S1). Notably, the catalytic performances of $CoCeO_x$-NP ($CoCeO_x$-0.5-NP, $CoCeO_x$-1-NP, and $CoCeO_x$-2-NP) are more active than CeO_2-NP and Co_3O_4-NP in toluene oxidation, and $CoCeO_x$-2-NP catalysts exhibited the highest toluene oxidation activity. This result implied that the Co-doped significantly improved the performance of the $CoCeO_x$-NP catalysts for toluene oxidation. It may be due to the synergistic effect between cobalt and cerium, which lead to the distortion of ceria lattice and produce oxygen vacancies, improving the oxidation performance of toluene [26]. Besides, the composition of the tail gas produced over the $CoCeO_x$-2-NP under the T_{90} reaction condition was analyzed, and the results of GC–MS (Figure S2) showed that the main content of the tail gas was CO_2 and a small amount of unreacted toluene. This is consistent with the good CO_2 selectivity of the $CoCeO_x$-2-NP catalyst (Figure S3). Meanwhile, compared to other catalysts, the $CoCeO_x$-2-NP still shows good catalytic performance for toluene oxidation (Table S2). Thus, the $CoCeO_x$-2-NP catalysts were selected as the best sample in the following performance experiments.

3.2. Structure and textural properties analysis

Fig. 1(B) presents the XRD patterns of samples. The peaks (2θ) at 28.6°, 33.2°, 47.6°, 56.4°, 59.1°, 69.4°, 76.7°, and 79.1° are the feature diffraction peaks of cubic CeO_2 (PDF#34–0394), which correspond to

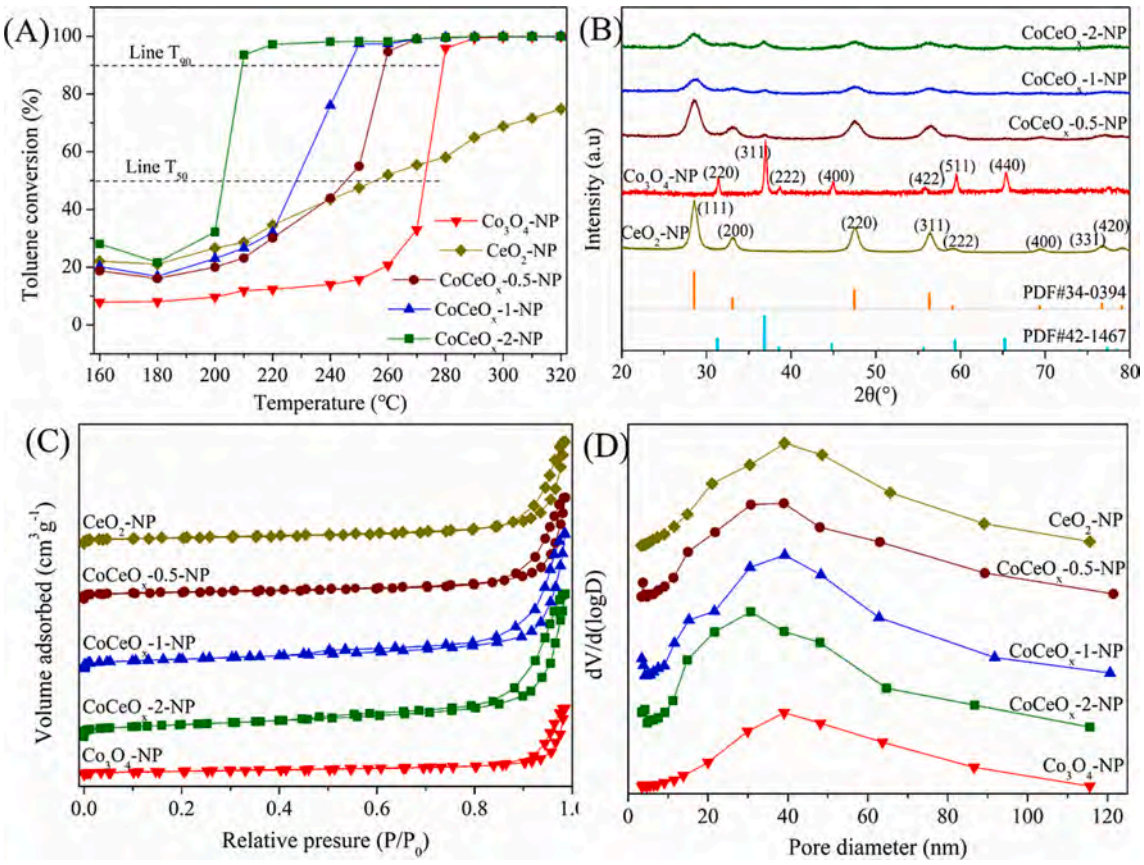

Fig. 1. (A) The toluene conversion performance over the catalysts, (B) XRD patterns of samples, (C) N_2 adsorption–desorption isotherms, (D) Pore size distributions of samples.

the planes of (111), (200), (220), (311), (222), (400), (331), and (420), respectively [27]. The Co_3O_4-NP showed a typical crystalline fluorite structure (PDF#42–1467), and the diffraction peaks (2θ) at 31.4°, 37°, 38.7°, 45°, 55.8°, 59.5°, and 65.4° could be assigned to the planes of (220), (311), (222), (400), (422), (511), and (440), respectively [28]. Compared with CeO_2-NP and Co_3O_4-NP, the diffraction pattern of $CoCeO_x$-0.5-NP, $CoCeO_x$-1-NP, and $CoCeO_x$-2-NP catalysts become broader and weaker. This result may be due to a certain amount of cobalt doping helping to disperse metals and causing the crystal size of $CoCeO_x$-NP to be smaller [26,29]. Table S1 shows that the crystal size of cobalt and cerium presents a decreasing trend with increased cobalt doping. Among them, the $CoCeO_x$-2-NP exhibited the smallest crystal size than other samples, facilitating the formation of more structural defects [30].

The N_2 adsorption–desorption isotherms and pore size distributions were performed to assist in understanding the structural characteristics of the samples. According to Fig. 1(C), all the samples exhibit the type-IV isotherms with H3 hysteresis loop at the relative pressure of 0.4 to 1.0, indicating that there is a mesoporous structure in the samples [30]. The pore size distribution of the samples is displayed in Fig. 1(D), and the pore diameter of CeO_2-NP, Co_3O_4-NP, $CoCeO_x$-0.5-NP, $CoCeO_x$-1-NP, and $CoCeO_x$-2-NP are mainly around 40, 39, 35,40, and 30 nm, respectively. Among them, $CoCeO_x$-2-NP showed the largest S_{BET} (55.2 m^2/g), the highest pore volume (0.3 m^3/g), and minor average pore diameter (19.9 nm) than other samples.

The SEM was characterized to understand the samples' morphology more intuitively (Figure S4). The template of PMMA presents spherical particles with uniform size (~120 nm) but disordered arrangement. Other samples showed disordered nanoparticles with some accumulations. The diameter sizes of CeO_2-NP and Co_3O_4-NP are around 65 and 50 nm. With the increase of Co doping, the diameter sizes of $CoCeO_x$-0.5-NP, $CoCeO_x$-1-NP, and $CoCeO_x$-2-NP were reduced to about 53, 46, and 40 nm, respectively, which may be due to the interaction between Co and Ce contributes to forming smaller particles to increase the exposure of active sites [31].

The crystal facets of different samples were obtained by HRTEM (Fig. 2). The lattice spacing of CeO_2 in all samples is around 0.32 nm, indicating that CeO_2 mainly exposes (111) crystal planes. Besides, with the increase of Co/Ce, the Co_3O_4 planes were found in $CoCeO_x$-1-NP and $CoCeO_x$-2-NP (Fig. 2(B)(C)). The lattice fringes spacing of 0.22 nm and 0.28 nm referred to (222) and (220) planes of Co_3O_4, indicating that cobalt was successfully doped into cerium dioxide. Notably, the sufficient contact of cobalt-cerium contributes to the exertion of synergistic effects [22,32].

3.3. Surface chemical properties and redox behavior

The information on element components, chemical states, and surface element content of samples was detected accurately by XPS. The results of the samples (CeO_2-NP, Co_3O_4-NP, $CoCeO_x$-0.5-NP, $CoCeO_x$-1-NP, and $CoCeO_x$-2-NP) about O 1s, Ce 3d, and Co 2p are shown in Fig. 3.

The O 1s of catalysts are shown in Fig. 3(A). The peaks at about 529.6 eV, 531.8 eV, and 533.2 eV are ascribed to lattice oxygen (O_α), adsorbed oxygen (O_β), and adsorbed water molecules or surface oxygen of hydroxyl species (O_{OH}), respectively [33,34]. The relative O_β content of the samples increased as follows (listed in Table 1): CeO_2-NP (17.2%) < Co_3O_4-NP (21.0%) < $CoCeO_x$-0.5-NP (22.4%) < $CoCeO_x$-1-NP (24.6%) < $CoCeO_x$-2-NP (32.9%), and the $CoCeO_x$-2-NP has the highest O_β content. This result suggested that in situ doping promotes oxygen vacancy formation and effectively increases the amount of O_β over the catalyst interface. The higher O_β content contributes to the low-temperature activity of the $CoCeO_x$-2-NP catalyst [35,36].

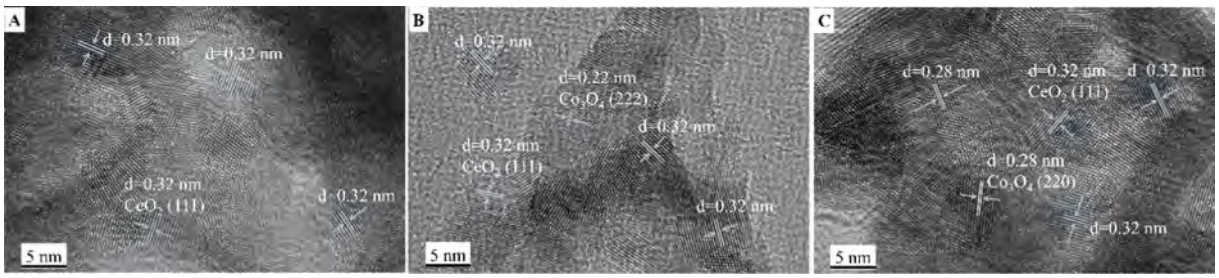

Fig. 2. HRTEM images of (A) $CoCeO_x$-0.5-NP, (B) $CoCeO_x$-1-NP, and (C) $CoCeO_x$-2-NP.

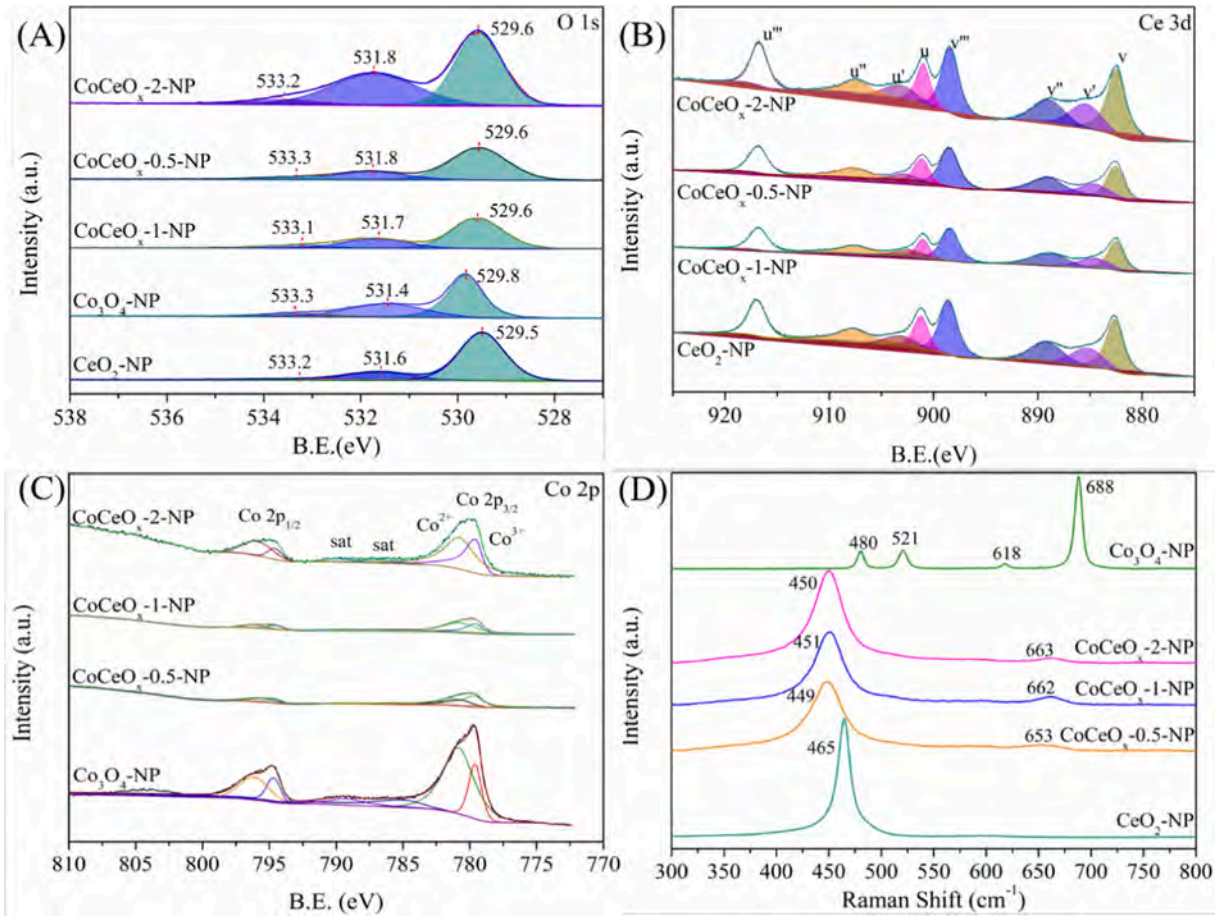

Fig. 3. The XPS spectra of (A) O1s, (B) Ce 3d, and (C) Co 2p, (D) Raman spectra.

Table 1
The relative surface element content of the samples.

Samples	Surface element contents (%)		
	$Ce^{3+}/(Ce^{3+}+Ce^{4+})$	$Co^{2+}/(Co^{2+}+Co^{3+})$	O_β/O_{tot} [a]
Co_3O_4-NP	–	37.5	21.0
CeO_2-NP	16.8	–	17.2
$CoCeO_x$-0.5-NP	16.4	41.6	22.4
$CoCeO_x$-1-NP	15.7	58.7	24.6
$CoCeO_x$-2-NP	20.1	59.0	32.9

[a] represent $O_{tot} = (O_\alpha + O_\beta + O_{OH})$.

The typical Ce 3d spectra of catalysts are shown in Fig. 3(B). The peaks of v' and u' could be assigned to Ce^{3+} species, and the peaks of v, v'', v''', and u, u'', u''' could be assigned to Ce^{4+} species [37]. The relative atomic content of Ce^{3+} was calculated by the formula of $Ce^{3+}/(Ce^{3+}+Ce^{4+})$, which is 16.8%, 16.4%, 15.7%, and 20.1% for CeO_2-NP, $CoCeO_x$-0.5-NP, $CoCeO_x$-1-NP, and $CoCeO_x$-2-NP, respectively. Among them, $CoCeO_x$-2-NP has the highest Ce^{3+} content than other samples. The high content of Ce^{3+} in the catalyst is usually accompanied by the formation of more oxygen vacancies [35,38], which is consistent with the results of O 1s.

Fig. 3(C) is the Co 2p XPS spectra of Co_3O_4-NP, $CoCeO_x$-0.5-NP, $CoCeO_x$-1-NP, and $CoCeO_x$-2-NP. The 780 eV and 795 eV peaks belonged to Co $2p_{1/2}$ and Co $2p_{3/2}$. The energy level difference value (ΔE) is generally believed at 15 eV [39]. Besides, the Co 2p spectrum contains two shake-up satellite peaks (denoted as sat) with low intensity were also observed around 786 eV and 790 eV. The Co $2p_{1/2}$ spectra were fitted into two peaks at 779.6 eV and 780.8 eV ascribed to Co^{3+} and Co^{2+}. For the Co $2p_{3/2}$ spectra, the 794.6 eV and 795.9 eV peaks were attributed to Co^{3+} and Co^{2+}, respectively, indicating that Co^{2+} and Co^{3+} coexist on the catalyst [40]. With the Co/Ce ratio increase, the content of low valence Co^{2+} showed a slight upward trend (except Co_3O_4-NP), which is conducive to forming oxygen vacancies [41].

The Raman spectra were performed to explore the oxygen vacancy information. As shown in Fig. 3(D), the Co_3O_4-NP led four typical Raman-active modes: E_g (480 cm^{-1}), F_{2g} (521 and 618 cm^{-1}), A_{1g} (688 cm^{-1}), which is good in line with Co_3O_4 spinel [42]. The CeO_2-NP exhibited a strong band at around 465 cm^{-1}, attributed to the cubic fluorite structure [43]. For the $CoCeO_x$ samples, the Raman shifts to lower frequencies and becomes wider with the increased Co/Ce ratio. This result indicated that Co was successfully incorporated into the CeO_2 lattice and promoted the generation of more oxygen vacancies over the interface of CeO_2 and Co_3O_4 [44,45]. Subsequently, the oxygen vacancies of samples were further evaluated by EPR. As shown in Figure S5, a symmetrical EPR signal at g = 2.003 was observed in the $CoCeO_x$-0.5-NP, $CoCeO_x$-1-NP, and $CoCeO_x$-2-NP, meaning that the generation of oxygen vacancies on the surface of $CoCeO_x$-NP samples prepared by cobalt doping [46,47]. Among them, the $CoCeO_x$-2-NP shows the highest concentration of oxygen vacancies. This is consistent with the results of XPS and Raman.

Generally, the reduction behavior of the samples has a great relationship with their oxygen species and the element valence state [40,48]. The H_2-TPR experiments were conducted to understand better the H_2-TPR profiles of the $CoCeO_x$-NP ($CoCeO_x$-0.5-NP, $CoCeO_x$-1-NP, and $CoCeO_x$-2-NP) (Fig. 4(A)). For reference, the CeO_2-NP and Co_3O_4-NP samples were also analyzed (Figure S6).

The peaks at 364 °C and 412 °C observed in the $CoCeO_x$-0.5-NP reduction profile were ascribed to the reduction of $Co^{3+}\rightarrow Co^{2+}\rightarrow Co$ [49], and the reduction peak at 210 °C, 277 °C, and 695 °C are assigned to surface oxygen species, subsurface oxygen, and bulk oxygen species of CeO_2, respectively [26]. Similar peaks were observed in samples $CoCeO_x$-1-NP and $CoCeO_x$-2-NP. Interestingly, compared with the Co_3O_4-NP and CeO_2-NP, the H_2-TPR profiles of the modified $CoCeO_x$-NP samples ($CoCeO_x$-0.5-NP, $CoCeO_x$-1-NP, and $CoCeO_x$-2-NP) are significantly shifted toward lower temperatures, and $CoCeO_x$-2-NP shifts more prominent. The results showed a synergistic effect between the cobalt and cerium interface and generated more oxygen species [50,51]. Moreover, the initial H_2 consumption rate versus reduction temperature (Figure S7) further indicated that $CoCeO_x$-2-NP had stronger reducibility than other samples [52,53].

O_2-TPD is an effective method to detect the mobility and type of oxygen species. Different oxygen species on the catalysts will be desorbed with the temperature increase. Usually, the physically adsorbed oxygen (O_{ads}) would be desorbed firstly (<150 °C); then the chemically adsorbed oxygen species (O_β) is desorbed (200–400 °C); finally, the lattice oxygen (O_α) is desorbed (>400 °C) [44,54,55]. According to Figure S8, four peaks were observed at around 108 °C, 309 °C, 448 °C, and 629 °C over the CeO_2-NP, the first two peaks were assigned to O_{ads} and O_β, respectively, and the last two peaks were attributed to O_α. For Co_3O_4-NP, the peak at 84 °C was attributed to O_{ads}. The peaks at 232 °C and 313 °C were assigned to O_β, and the last peak at 834 °C belonged to O_α.

Notably, the O_β of $CoCeO_x$ ($CoCeO_x$-0.5-NP, $CoCeO_x$-1-NP, and $CoCeO_x$-2-NP) in Fig. 4(B) was significantly stronger than that of Co_3O_4 and CeO_2, which may be due to the interaction between the cobalt-cerium interface and oxygen vacancies created on the catalyst surface improve the mobility of oxygen species [45,56]. A significant increase of chemically adsorbed oxygen species was observed on the $CoCeO_x$-2-NP catalysts, consistent with the XPS results. This result is related to the fact that cobalt doping promotes the formation of more oxygen vacancies at the interface between Co_3O_4 and CeO_2, which is conducive to activating the lattice oxygen and improving its mobility, thus forming more reactive oxygen species [49,57,58].

3.4. *The effects of operating conditions (WHSV, water vapor, and toluene concentrations), stability, and reusability on toluene oxidation over the $CoCeO_x$-2-NP catalysts*

The space velocity directly determines the residence time of the reactants on the surface of the catalyst. The effect of different WHSVs on toluene oxidation is shown in Fig. 5(A). With the increase of WHSV, the T_{90} presents a gradual upward trend, and the T_{90} at 60 000 $mL{\cdot}h^{-1}{\cdot}g^{-1}$, 90 000 $mL{\cdot}h^{-1}{\cdot}g^{-1}$, and 180 000 $mL{\cdot}h^{-1}{\cdot}g^{-1}$ are 209 °C, 218 °C, and 236 °C, respectively. This phenomenon meant that the low WHSV improved the contact between toluene and the active sites and positively affected toluene oxidation over $CoCeO_x$-2-NP catalysts. The effect of different water content (5%, 10 vol%, 15 vol%, and 20 vol%) on toluene oxidation showed that the conversion efficiency of toluene decreased gradually with the increase of water content (Fig. 5(B)). It can be seen that there is a slight change in the conversion efficiency of toluene when 5 vol% H_2O is added. However, the conversion efficiency decreased to 91%, 81%, and 75% after further increased H_2O content to 10 vol%, 15 vol%, and 20 vol%, respectively. This inhibitory trend was mainly caused by the competitive adsorption between water vapor and toluene on the surface of $CoCeO_x$-2-NP and became more evident with the water content increased [30,59]. The H_2O transient response experiment (Figure S9) further shows that the inhibition of H_2O on catalytic oxidation of toluene by $CoCeO_x$-2-NP catalysts is temporary [6]. Subsequently, the effect of different toluene concentrations (500, 1000, and 1500 ppm) on catalyst activity was evaluated. As shown in Figure S10 (A), the catalytic activity of the $CoCeO_x$-2-NP at 220 °C was similar at three different toluene concentration gradients, and the conversion efficiency of toluene still exceeds 96%. This result suggested that the $CoCeO_x$-2-NP catalysts had sufficient active sites and maintained a wide range of toluene treatment capacity. Besides, the temperature cycling experiment indicated that the $CoCeO_x$-2-NP catalysts exhibited good thermal stability for toluene oxidation with the change of temperatures

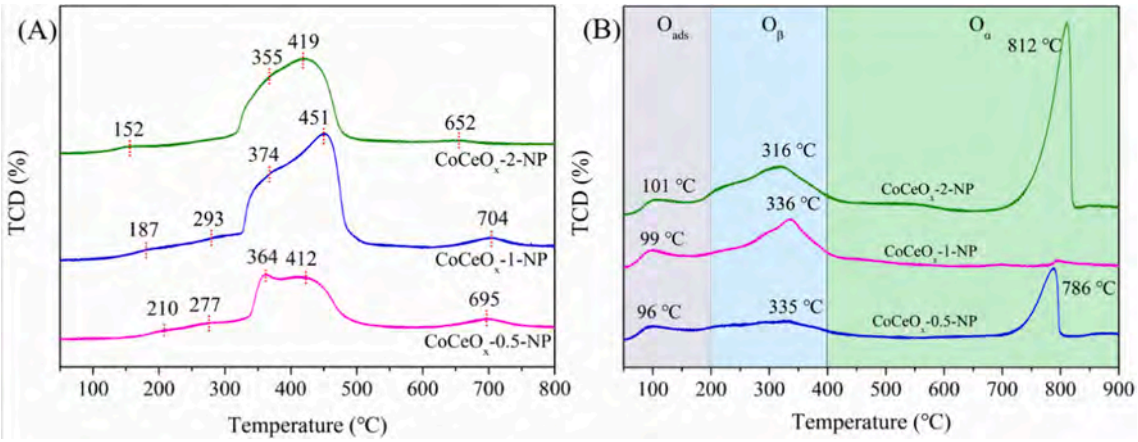

Fig. 4. (A) H_2-TPR profile and (B) O_2-TPD profiles of the catalysts.

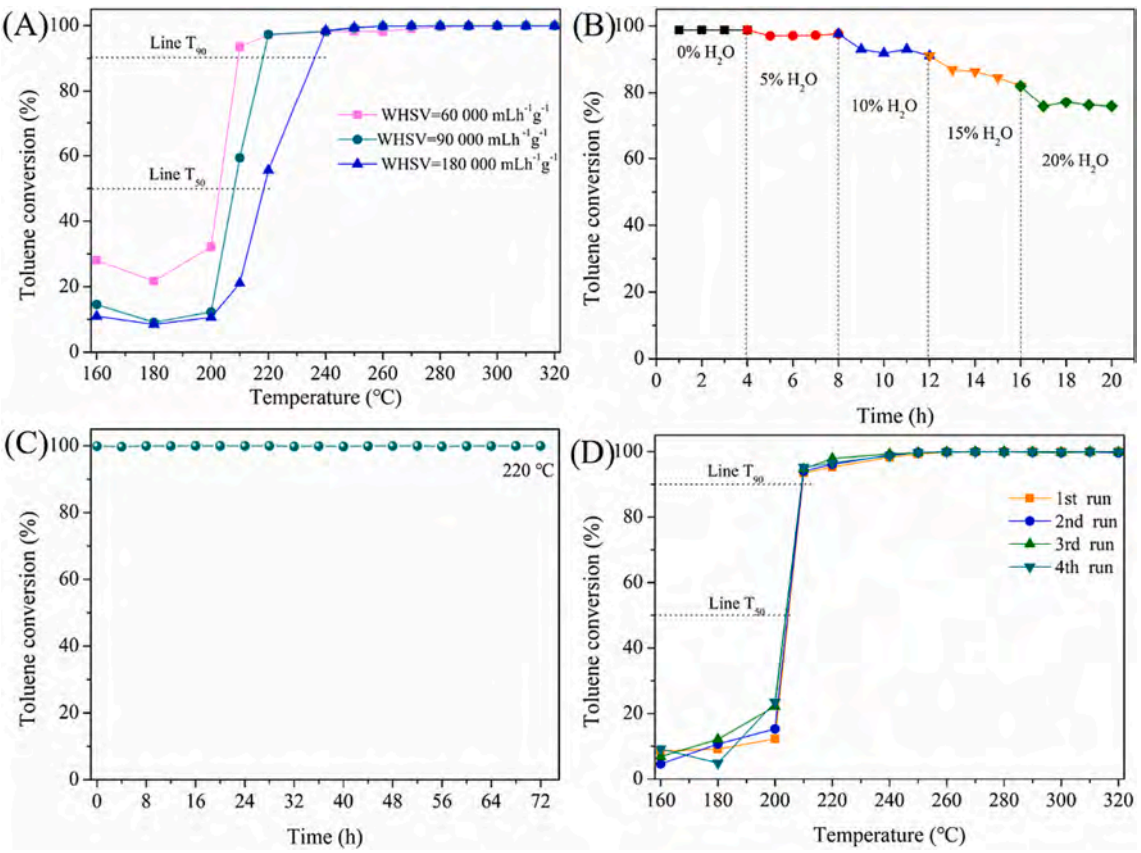

Fig. 5. The effects of WHSV (A) and H_2O (B) on toluene conversion over the $CoCeO_x$-2-NP catalysts. The stability (C) and reusability (D) of $CoCeO_x$-2-NP catalysts for toluene oxidation.

(Figure S10(B)).

As one of the essential parameters for evaluating the quality of catalysts, stability is related to industrial applications. As shown in Fig. 5 (C), the $CoCeO_x$-2-NP catalyst exhibits excellent stability (>99%) for toluene oxidation at 220 °C, and no significant fluctuations were observed during the 72 h continuous long-term durability experiment. To further check the durability of the catalyst, the toluene oxidation reaction was conducted at T_{50}. As shown in Figure S11(A), the conversion efficiency of toluene gradually decreased with the extension of the reaction time. After 72 h of reaction, the catalytic efficiency remained at 40%. Subsequently, further compared and analyzed the carbon deposition on the $CoCeO_x$-2-NP-fresh and $CoCeO_x$-2-NP-used surface by FTIR (Figure S11(B)). By comparing the $CoCeO_x$-2-NP-fresh and $CoCeO_x$-2-NP-used samples, two distinct peaks attributed to maleic anhydride (1306 cm^{-1}) and aromatic ring (1460 cm^{-1}) were observed in $CoCeO_x$-2-NP-used samples [60]. The results showed that the gradual deactivation of the catalyst was mainly caused by the incomplete oxidation of toluene, which caused carbon deposition (mainly maleic anhydride and aromatic ring species) on the catalyst surface, resulting in the coverage of active sites [61].

Besides, the reusability is related to the cost of operation and whether the production is environmentally friendly and energy-efficient. Therefore, the four continuous cycling experiments were conducted over $CoCeO_x$-2-NP catalysts (Fig. 5(D)). T_{50} and T_{90} of the samples exhibited high repeatability at around 203 °C and 209 °C, indicating that the $CoCeO_x$-2-NP catalysts have excellent reusability and potential application prospects for toluene oxidation.

3.5. The mechanism of toluene oxidation over $CoCeO_x$-2-NP

Detecting intermediate species is essential for a deeper understanding of the pathway of toluene oxidation, so the in situ DRIFTS experiment was first conducted on the $CoCeO_x$-2-NP catalysts under 1000 ppm toluene + N_2 conditions. As shown in Figure S12, the bands belonged to C = C of aromatic ring (1610 cm^{-1}) and C–H of alkyl group (2934 and 2970 cm^{-1}), meaning that toluene was adsorbed on the surface of $CoCeO_x$-2-NP [35,62,63]. Notably, the peak at 1433 and 1506 cm-1 is attributed to C = C of aromatic ring gradually disappearing [64,65]. However, the bands assigned to benzyl alcohol (1076, 1241, 1275, and 1362 cm^{-1}) and the benzaldehyde species (1478 cm^{-1}) [48,66–69] are gradually strengthening with the temperature increases (200–280 °C), indicating that toluene has been oxidized into intermediate products and gradually accumulates on the surface of the catalyst. This result is associated with increasing the temperature is beneficial for activating more lattice oxygen to participate in the oxidation of toluene, thereby improving the catalytic performance of $CoCeO_x$-2-NP for toluene oxidation [23,69].

In situ DRIFTS experiments were conducted on the $CoCeO_x$-2-NP catalysts under 1000 ppm toluene + air conditions to verify the role of reactive oxygen species in the reaction process. As shown in Fig. 6(A)(A-1), the absorption bands can be quickly observed after feed gas (1000 ppm toluene + 20 vol% O_2 + balance N_2) was introduced into the IR system, and the skeletal vibration of the aromatic ring observed at 1448, 1492, and 1524 cm^{-1} [60,70]. The bands at 3045 and 3072 cm^{-1} are the characteristics of C–H stretching vibrations in benzene rings. The weak stretching vibration of C–H (asymmetric or symmetric) in methylene was also detected at 2882 and 2934 cm^{-1} [53,71]. The above results indicated that toluene was adsorbed on the surface of $CoCeO_x$-2-NP catalysts. With the extension of reaction time, more bands were observed. Such as, the bands at 1025, 1068, and 1179 cm^{-1} belonged to alkoxide species (C-O) [60], and the C = O stretching vibration of aldehydic species was observed at 1654 cm^{-1} [53]. This result meant

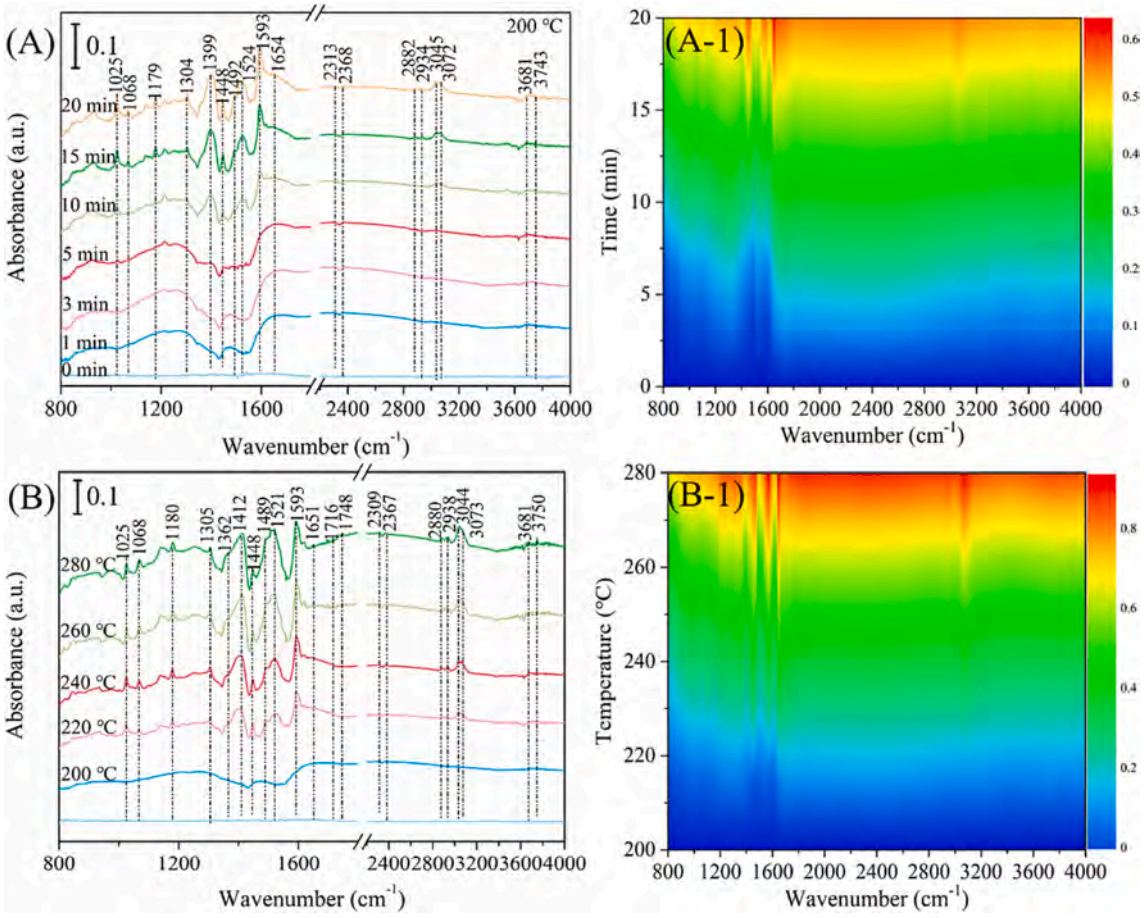

Fig. 6. In situ DRIFTS of $CoCeO_x$-2-NP catalysts exposure to toluene in air at (A)(A-1) different adsorption time and (B)(B-1) different temperatures.

that toluene had been oxidized into benzyl alcohol and benzaldehyde. Besides, the strong bands at 1399 and 1593 cm^{-1} are the typical carboxylate group, implying that benzoate species were further formed [72]. The band located at 1304 cm^{-1} could be attributed to maleic anhydride species [60]. The final product of CO_2 was also observed at 2313 and 2368 cm^{-1} [73]. The results of GC–MS (Figure S2) further confirmed the existence of corresponding intermediates in the oxidation of toluene. In addition, the intensity of the bands becomes stronger with the prolongation of the reaction time, suggesting that the intermediates formed during toluene oxidation and gradually accumulated on the surface of $CoCeO_x$-2-NP catalysts.

Fig. 6(B)(B-1) shows the absorption bands over the $CoCeO_x$-2-NP catalysts at different temperatures (200–280 °C). As the reaction temperature increases, more intermediates can be detected, and their intensity gradually strengthens. When the temperature exceeds 240 °C, the strength of bands almost remains unchanged, which may be due to the oxidation of toluene to achieve dynamic equilibrium. It is worth noting that the band attributed to the carboxylic acids (C = O stretching vibrations) at 1716 cm^{-1} gradually appeared with the temperature increase [74], indicating that high temperature contributes to the catalytic decomposition of toluene, agreeing with the toluene conversion results (Fig. 1A).

To further explore the role of oxygen species in toluene oxidation over the fresh and used $CoCeO_x$-2-NP, the O 1s XPS spectra were characterized (Figure S13). Three peaks can be fitted at around 529.6 eV, 531.7 eV, and 533.2 eV, which were assigned to O_α, O_β, and O_{OH}, respectively [34]. The detailed information is summarized in Table S3. For $CoCeO_x$-2-NP-fresh, the O_α/O_{tot} and O_β/O_{tot} are 56.8% and 32.9%, respectively, higher than the $CoCeO_x$-2-NP-used, implying that O_α and O_β have participated in the oxidation of toluene. Besides, the O_{OH}/O_{tot} increased from 10.3% to 17.4% after the reaction, which may be caused by the formation of H_2O during toluene oxidation.

Subsequently, DFT calculation was used to assist the mechanism study of toluene oxidation. Specifically, to understand the adsorption effect of the intermediates on the catalyst, we constructed adsorption models of different intermediate species at the interface of CeO_2 and Co_3O_4. As shown in Fig. 7, it can be observed that benzyl alcohol, benzaldehyde, benzoic acid, and maleic anhydride are more easily adsorbed at the interface of $CoCeO_x$-NP than toluene. Although the E_{ads} of benzoic acid is lower than that of benzaldehyde and maleic anhydride, it can be further found from Figure S14 that the accumulation of benzoic acid on the catalyst surface increases rapidly with the extension of time, indicating that benzoic acid is an important intermediate in the oxidation of toluene.

According to the above results, the toluene oxidation over the $CoCeO_x$-NP catalysts could be described as follows (Fig. 7): toluene was first adsorbed on the surface of catalysts, then reacted with reactive oxygen species (O_α and O_β) and oxidized to benzyl alcohol, benzaldehyde species, and benzoic acid, respectively. Subsequently, the aromatic ring of benzoic acid was opened under the action of reactive oxygen species, and the maleate species formed. Finally, the reactive oxygen species further oxidized the intermediates species to generate CO_2 and H_2O. The surface oxygen species consumed during the reaction process can be effectively replenished by gaseous oxygen (O_2). The intermediate species (including benzyl alcohol, benzaldehyde, and benzoic acid) have been detected before cracking the aromatic ring.

In contrast, a few intermediate species were seen after the benzene ring opening. It can be inferred that the cracking of the aromatic ring is the primary rate control step in the catalytic oxidation process of toluene [32,75]. Based on the results of XPS and the O_2-TPD, it can be speculated

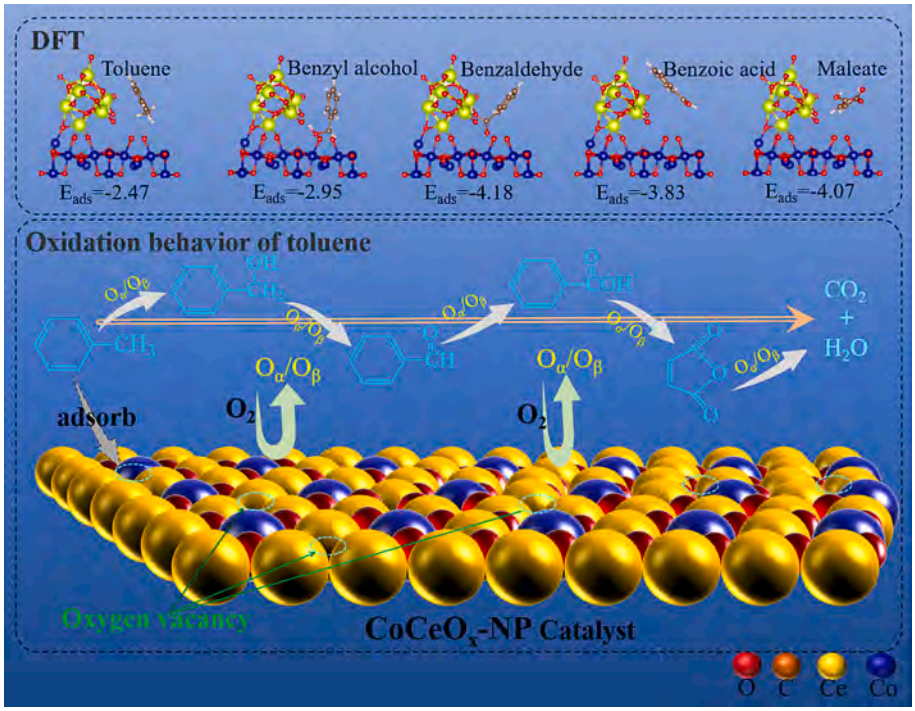

Fig. 7. The mechanism of toluene oxidation over the $CoCeO_x$-NP catalyst.

that the catalytic oxidation reaction of toluene on $CoCeO_x$-NP catalyst mainly involves O_β at low temperatures. With the reaction temperature increases, O_α is gradually activated, and the oxygen species participating in the reaction gradually transform into O_α. Therefore, the catalytic oxidation process of toluene on $CoCeO_x$-NP catalyst maybe follows the Langmuir-Hinshelwood (L-H) mechanism and Mars-van Krevelen (MvK) mechanism.

4. Conclusions

In this work, the $CoCeO_x$-NP catalysts were prepared by the template method for toluene oxidation. An interfacial synergistic effect was found between cobalt and cerium during toluene oxidation. Furthermore, appropriate Co-doped helps increase the specific surface area and enhance the mobility of oxygen species, which have greatly improved the low temperatures reducibility of $CoCeO_x$-NP catalysts. $CoCeO_x$-2-NP exhibited the highest catalytic performance ($T_{50} = 203\ ^\circ C$, $T_{90} = 209\ ^\circ C$) and CO_2 selectivity. Besides, the $CoCeO_x$-2-NP catalysts exhibited excellent stability and reusability, making it a high potential for practical applications in VOCs control. O_α and O_β played a crucial role in toluene oxidation. Cracking the aromatic ring is an essential step in completely oxidizing toluene. Moreover, the combined analysis of in situ DRIFTS and XPS indicated that the toluene oxidation over the $CoCeO_x$-NP catalyst might follow both the L-H and MvK mechanism.

CRediT authorship contribution statement

Youcai Zhu: Investigation, Data curation, Visualization, Methodology, Writing – original draft. **Caiting Li:** Conceptualization, Validation, Writing – review & editing, Project administration, Funding acquisition. **Xuan Liu:** Writing – review & editing. **Ying Zhang:** Investigation. **Kuang Yang:** Investigation. **Le Huang:** Investigation. **Jungang Zhao:** Data curation, Methodology. **Ziang Zhang:** Data curation, Methodology.

Declaration of Competing Interest

The authors declare that they have no known competing financial interests or personal relationships that could have appeared to influence the work reported in this paper.

Data availability

Data will be made available on request.

Acknowledgments

This work was supported by the National Natural Science Foundation of China (52270102), the Key Research and Development Program of Hunan Province in China (2018SK2032), and the National Key Research and Development Program of China (2016YFC0204100).

Appendix A. Supplementary data

Supplementary data to this article can be found online at https://doi.org/10.1016/j.seppur.2023.124993.

References

[1] C. He, J. Cheng, X. Zhang, M. Douthwaite, S. Pattisson, Z. Hao, Recent advances in the catalytic oxidation of volatile organic compounds: A review based on pollutant sorts and sources, Chem. Rev. 119 (2019) 4471–4568.
[2] M.S. Kamal, S.A. Razzak, M.M. Hossain, Catalytic oxidation of volatile organic compounds (VOCs) – A review, Atmo. Environ. 140 (2016) 117–134.
[3] H. Yi, X.i. Yang, X. Tang, S. Zhao, X. Xie, T. Feng, Y. Ma, X. Cui, Performance and pathways of toluene degradation over Co/13X by different processes based on nonthermal plasma, Energy. Fuel 31 (10) (2017) 11217–11224.
[4] X. Yu, X.Q. Dang, S.J. Li, J.L. Zhang, Q. Zhang, L. Cao, A comparison of in- and post-plasma catalysis for toluene abatement through continuous and sequential processes in dielectric barrier discharge reactors, J. Clean. Prod. 276 (2020), 124251.
[5] J. Zhu, J. Sun, S. Tian, J. Yang, J. Feng, Y.a. Xiong, Catalytic activity and mechanism of fluorinated MgO film supported on 3D nickel mesh for ozonation of gaseous toluene, Environ. Sci. Nano 7 (9) (2020) 2723–2734.
[6] Y. Luo, D. Lin, Y. Zheng, X. Feng, Q. Chen, K. Zhang, X. Wang, L. Jiang, MnO_2 nanoparticles encapsuled in spheres of Ce-Mn solid solution: Efficient catalyst and

good water tolerance for low-temperature toluene oxidation, Appl. Surf. Sci. 504 (2020), 144481.
[7] R.S. Peng, S.J. Li, X.B. Sun, Q.M. Ren, L.M. Chen, M.L. Fu, J.L. Wu, D.Q. Ye, Size effect of pt nanoparticles on the catalytic oxidation of toluene over pt/CeO_2 catalysts, Appl. Catal. B: Environ. 220 (2018) 462–470.
[8] J.R. Li, W.P. Zhang, C. Li, C. He, Efficient catalytic degradation of toluene at a readily prepared Mn-Cu catalyst: Catalytic performance and reaction pathway, J. Colloid Interface Sci. 591 (2021) 396–408.
[9] M. Xiao, X. Yu, Y. Guo, M. Ge, Boosting toluene combustion by tuning electronic Metal-Support interactions in In situ grown pt@Co_3O_4 Catalysts, Environ. Sci. Tech. 56 (2) (2022) 1376–1385.
[10] S. Xie, J. Deng, S. Zang, H. Yang, G. Guo, H. Arandiyan, H. Dai, Au-Pd/3DOM Co_3O_4: Highly active and stable nanocatalysts for toluene oxidation, J. Catal. 322 (2015) 38–48.
[11] Y. Lyu, C.T. Li, X.Y. Du, Y.C. Zhu, Y.D. Zhang, S.H. Li, Catalytic oxidation of toluene over mnO_2 catalysts with different mn (II) precursors and the study of reaction pathway, Fuel 262 (2020), 116610.
[12] F.J. Shi, F. Wang, H.X. Dai, J.X. Dai, J.G. Deng, Y.X. Liu, G.M. Bai, K.M. Ji, C.T. Au, Rod-, flower-, and dumbbell-like MnO_2: Highly active catalysts for the combustion of toluene, Appl. Catal. A 433 (2012) 206–213.
[13] W.B. Pei, Y.X. Liu, J.G. Deng, K.F. Zhang, Z.Q. Hou, X.T. Zhao, H.X. Dai, Partially embedding pt nanoparticles in the skeleton of 3DOM mn_2O_3: An effective strategy for enhancing catalytic stability in toluene combustion, Appl. Catal. B: Environ. 256 (2019), 117814.
[14] Z. Abdelouahab-Reddam, R. El Mail, F. Coloma, A. Sepulveda-Escribano, Platinum supported on highly-dispersed ceria on activated carbon for the total oxidation of VOCs, Appl. Catal. A 494 (2015) 87–94.
[15] J. Chen, X. Chen, W.J. Xu, Z. Xu, J.Z. Chen, H.P. Jia, J. Chen, Hydrolysis driving redox reaction to synthesize Mn-Fe binary oxides as highly active catalysts for the removal of toluene, Chem. Eng. J. 330 (2017) 281–293.
[16] H. Li, C.-Y. Wu, Y. Li, J. Zhang, CeO_2-TiO_2 catalysts for catalytic oxidation of elemental mercury in low-rank coal combustion flue gas, Environ. Sci. Tech. 45 (17) (2011) 7394–7400.
[17] Y. Zhu, C. Li, Y. Lyu, S. Li, Y. Zhang, X. Du, Y. Zhai, Insight into the effect of SO_2 on the Hg0 removal performance over a 1V–8Ce/AC sorbent at low temperatures, J. Hazard. Mater. 402 (2021), 123502.
[18] Y.C. Zhu, X.J. Han, Z.G. Huang, Y.Q. Hou, Y.P. Guo, M.H. Wu, Superior activity of CeO_2 modified V_2O_5/AC catalyst for mercury removal at low temperature, Chem. Eng. J. 337 (2018) 741–749.
[19] P. Yang, S.S. Yang, Z.N. Shi, Z.H. Meng, R.X. Zhou, Deep oxidation of chlorinated VOCs over CeO_2-based transition metal mixed oxide catalysts, Appl. Catal. B: Environ. 162 (2015) 227–235.
[20] W.B. Pei, L.Y. Dai, Y.X. Liu, J.G. Deng, L. Jing, K.F. Zhang, Z.Q. Hou, Z. Han, A. Rastegarpanah, H.X. Dai, PtRu nanoparticles partially embedded in the 3DOM $ce_{0.7}Zr_{0.3}O_2$ skeleton: Active and stable catalysts for toluene combustion, J. Catal. 385 (2020) 274–288.
[21] Q. Yan, X. Li, Q. Zhao, G. Chen, Shape-controlled fabrication of the porous Co_3O_4 nanoflower clusters for efficient catalytic oxidation of gaseous toluene, J. Hazard. Mater. 209–210 (2012) 385–391.
[22] W. Fang, J. Chen, X. Zhou, J. Chen, Z. Ye, J. Li, Zeolitic imidazolate Framework-67-Derived CeO_2@Co_3O_4 Core-Shell Microspheres with Enhanced Catalytic Activity toward Toluene Oxidation, Ind. Eng. Chem. Res. 59 (22) (2020) 10328–10337.
[23] X. Feng, F. Luo, Y. Chen, D. Lin, Y. Luo, L. Xiao, X. Liu, X. Sun, Q. Qian, Q. Chen, Boosting total oxidation of propane over CeO_2@Co_3O_4 nanofiber catalysts prepared by multifluidic coaxial electrospinning with continuous grain boundary and fast lattice oxygen mobility, J. Hazard. Mater. 406 (2021), 124695.
[24] K.M. Ji, H.X. Dai, J.X. Dai, J.G. Deng, F. Wang, H. Zhang, L. Zhang, PMMA-templating preparation and catalytic activities of three-dimensional macroporous strontium ferrites with high surface areas for toluene combustion, Catal. Today 201 (2013) 40–48.
[25] W. Si, Y.u. Wang, S. Zhao, F. Hu, J. Li, A facile method for in situ preparation of the MnO_2/$LaMnO_3$ Catalyst for the Removal of Toluene, Environ. Sci. Tech. 50 (8) (2016) 4572–4578.
[26] F.Y. Hu, Y. Peng, J.J. Chen, S. Liu, H. Song, J.H. Li, Low content of CoO_x supported on nanocrystalline CeO_2 for toluene combustion: The importance of interfaces between active sites and supports, Appl. Catal. B: Environ. 240 (2019) 329–336.
[27] J.P. Du, Z.P. Qu, C. Dong, L.X. Song, Y. Qin, N. Huang, Low-temperature abatement of toluene over Mn-Ce oxides catalysts synthesized by a modified hydrothermal approach, Appl. Surf. Sci. 433 (2018) 1025–1035.
[28] Q.M. Ren, Z.T. Feng, S.P. Mo, C.L. Huang, S.J. Li, W.X. Zhang, L.M. Chen, M.L. Fu, J.L. Wu, D.Q. Ye, 1D-Co_3O_4, 2D-Co_3O_4, 3D-Co_3O_4 for catalytic oxidation of toluene, Catal. Today 332 (2019) 160–167.
[29] Z.T. Feng, Q.M. Ren, R.S. Peng, S.P. Mo, M.Y. Zhang, M.L. Fu, L.M. Chen, D.Q. Ye, Effect of CeO_2 morphologies on toluene catalytic combustion, Catal. Today 332 (2019) 177–182.
[30] F. Hu, J. Chen, Y. Peng, H. Song, K. Li, J. Li, Novel nanowire self-assembled hierarchical CeO_2 microspheres for low temperature toluene catalytic combustion, Chem. Eng. J. 331 (2018) 425–434.
[31] L.L. Zhao, Z.P. Zhang, Y.S. Li, X.S. Leng, T.R. Zhang, F.L. Yuan, X.Y. Niu, Y.J. Zhu, Synthesis of ce_aMnO_x hollow microsphere with hierarchical structure and its excellent catalytic performance for toluene combustion, Appl. Catal. B: Environ. 245 (2019) 502–512.
[32] Y. Shen, J. Deng, S. Impeng, S. Li, T. Yan, J. Zhang, L. Shi, D. Zhang, Boosting toluene combustion by engineering Co-O strength in cobalt oxide catalysts, Environ. Sci. Tech. 54 (16) (2020) 10342–10350.
[33] S.D. Li, H.S. Wang, W.M. Li, X.F. Wu, W.X. Tang, Y.F. Chen, Effect of cu substitution on promoted benzene oxidation over porous cuCo-based catalysts derived from layered double hydroxide with resistance of water vapor, Appl. Catal. B: Environ. 166 (2015) 260–269.
[34] K. Yang, Y.X. Liu, J.G. Deng, X.T. Zhao, J. Yang, Z. Han, Z.Q. Hou, H.X. Dai, Three-dimensionally ordered mesoporous iron oxide-supported single-atom platinum: Highly active catalysts for benzene combustion, Appl. Catal. B: Environ. 244 (2019) 650–659.
[35] X. Chen, X. Chen, E.Q. Yu, S.C. Cai, H.P. Jia, J. Chen, P. Liang, In situ pyrolysis of Ce-MOF to prepare CeO_2 catalyst with obviously improved catalytic performance for toluene combustion, Chem. Eng. J. 344 (2018) 469–479.
[36] B. Li, Q.L. Yang, Y. Peng, J.J. Chen, L. Deng, D. Wang, X.W. Hong, J.H. Li, Enhanced low-temperature activity of $LaMnO_3$ for toluene oxidation: The effect of treatment with an acidic $KMnO_4$, Chem. Eng. J. 366 (2019) 92–99.
[37] Z.T. Feng, M.Y. Zhang, Q.M. Ren, S.P. Mo, R.S. Peng, D.F. Yan, M.L. Fu, L.M. Chen, J.L. Wu, D.Q. Ye, Design of 3-dimensionally self-assembled CeO_2 hierarchical nanosphere as high efficiency catalysts for toluene oxidation, Chem. Eng. J. 369 (2019) 18–25.
[38] R.S. Peng, X.B. Sun, S.J. Li, L.M. Chen, M.L. Fu, J.L. Wu, D.Q. Ye, Shape effect of Pt/CeO_2 catalysts on the catalytic oxidation of toluene, Chem. Eng. J. 306 (2016) 1234–1246.
[39] F.-X. Ma, L.e. Yu, C.-Y. Xu, X.W.(. Lou, Self-supported formation of hierarchical $NiCo_2O_4$ tetragonal microtubes with enhanced electrochemical properties, Energy. Environ. Sci. 9 (3) (2016) 862–866.
[40] Q. Ren, S. Mo, R. Peng, Z. Feng, M. Zhang, L. Chen, M. Fu, J. Wu, D. Ye, controllable synthesis of 3D hierarchical co_3O_4 nanocatalysts with various morphologies for the catalytic oxidation of toluene, J. Mater. Chem. A 6 (2) (2018) 498–509.
[41] K. Li, R.R. Zhang, R.J. Gao, G.Q. Shen, L. Pan, Y.D. Yao, K.H. Yu, X.W. Zhang, J. J. Zou, Metal-defected spinel $mn_xCo_{3-x}O_4$ with octahedral mn-enriched surface for highly efficient oxygen reduction reaction, Appl. Catal. B: Environ. 244 (2019) 536–545.
[42] E. Rios, P. Chartier, J.L. Gautier, Oxygen evolution electrocatalysis in alkaline medium at thin $MnxCo_{3-x}O_4$ ($0 \leq x \leq 1$) spinel films on glass/SnO_2: F prepared by spray pyrolysis, Solid. State. Sci. 1 (1999) 267–277.
[43] D. Mukherjee, B.G. Rao, B.M. Reddy, CO and soot oxidation activity of doped ceria: Influence of dopants, Appl. Catal. B: Environ. 197 (2016) 105–115.
[44] T. Cai, H. Huang, W. Deng, Q.G. Dai, W. Liu, X.Y. Wang, Catalytic combustion of 1,2-dichlorobenzene at low temperature over mn-modified Co_3O_4 catalysts, Appl. Catal. B: Environ. 166 (2015) 393–405.
[45] A. Ismail, M. Li, M. Zahid, L. Fan, C. Zhang, Z. Li, Y. Zhu, Effect of strong interaction between co and ce oxides in $co_xCe_{1-x}O_{2-\delta}$ oxides on its catalytic oxidation of toluene, Mole. Catal. 502 (2021), 111356.
[46] Y. Zheng, Y. Su, C. Pang, L. Yang, C. Song, N.a. Ji, D. Ma, X. Lu, R. Han, Q. Liu, Interface-Enhanced oxygen vacancies of $CoCuO_x$ Catalysts In Situ Grown on Monolithic Cu Foam for VOC Catalytic Oxidation, Environ. Sci. Tech. 56 (3) (2022) 1905–1916.
[47] S.P. Mo, Q. Zhang, J.Q. Li, Y.H. Sun, Q.M. Ren, S.B. Zou, Q. Zhang, J.H. Lu, M. L. Fu, D.Q. Mo, J.L. Wu, H.M. Huang, D.Q. Ye, Highly efficient mesoporous MnO_2 catalysts for the total toluene oxidation: Oxygen-Vacancy defect engineering and involved intermediates using in situ DRIFTS, Appl. Catal. B: Environ. 264 (2020), 118464.
[48] R.L. Mi, D. Li, Z. Hu, R.T. Yang, Morphology effects of CeO_2 Nanomaterials on the Catalytic Combustion of Toluene: A Combined Kinetics and Diffuse Reflectance Infrared Fourier Transform Spectroscopy Study, ACS Catal. 11 (2021) 7876–7889.
[49] X.Y. Feng, J.X. Guo, X.R. Wen, M.Y. Xu, Y.H. Chu, S.D. Yuan, Enhancing performance of Co/CeO_2 catalyst by Sr doping for catalytic combustion of toluene, Appl. Surf. Sci. 445 (2018) 145–153.
[50] Q. Ren, S. Mo, J. Fan, Z. Feng, M. Zhang, P. Chen, J. Gao, M. Fu, L. Chen, J. Wu, D. Ye, Enhancing catalytic toluene oxidation over MnO_2@Co_3O_4 by constructing a coupled interface, Chinese, J. Catal. 41 (12) (2020) 1873–1883.
[51] W. Liu, J. Fan, Z. Song, X. Zhang, Preparation of mesoporous ce_xCoO as highly effective catalysts for toluene combustion: the synergetic effects of structural template and ce doping, Appl. Organomet. Chem. 35 (1) (2021).
[52] J. Deng, S. He, S. Xie, H. Yang, Y. Liu, G. Guo, H. Dai, Ultralow loading of silver nanoparticles on mn_2O_3 Nanowires Derived with Molten Salts: A High-Efficiency Catalyst for the Oxidative Removal of Toluene, Environ. Sci. Tech. 49 (2015) 11089–11095.
[53] S. Zhao, F. Hu, J. Li, Hierarchical Core-Shell Al_2O_3@Pd-CoAlO microspheres for Low-Temperature toluene combustion, ACS Catal. 6 (6) (2016) 3433–3441.
[54] M.H. Castaño, R. Molina, S. Moreno, Cooperative effect of the Co-Mn mixed oxides for the catalytic oxidation of VOCs: Influence of the synthesis method, Appl. Catal. A 492 (2015) 48–59.
[55] B. Chen, B.o. Wu, L. Yu, M. Crocker, C. Shi, Investigation into the catalytic roles of various oxygen species over different crystal phases of MnO_2 for C_6H_6 and HCHO Oxidation, ACS Catal. 10 (11) (2020) 6176–6187.
[56] W. Han, H. Zhao, F. Dong, Z. Tang, Morphology-controlled synthesis of 3D, mesoporous, rosette-like $CeCoO_x$ catalysts by pyrolysis of Ce[$Co(CN)_6$] and application for the catalytic combustion of toluene, Nanoscale 10 (45) (2018) 21307–21319.
[57] Z. Su, W. Yang, C. Wang, S. Xiong, X. Cao, Y. Peng, W. Si, Y. Weng, M. Xue, J. Li, Roles of oxygen vacancies in the bulk and surface of CeO_2 for Toluene Catalytic Combustion, Environ. Sci. Tech. 54 (19) (2020) 12684–12692.
[58] F. Esch, S. Fabris, L. Zhou, T. Montini, C. Africh, P. Fornasiero, G. Comelli, R. Rosei, Electron localization determines defect formation on ceria substrates, Science 309 (5735) (2005) 752–755.

[59] S. Xie, H. Dai, J. Deng, Y. Liu, H. Yang, Y. Jiang, W. Tan, A. Ao, G. Guo, Au/3DOM co_3O_4: highly active nanocatalysts for the oxidation of carbon monoxide and toluene, Nanoscale 5 (2013) 11207–11219.
[60] C. Dong, Z.P. Qu, Y. Qin, Q. Fu, H.C. Sun, X.X. Duan, Revealing the highly catalytic performance of spinel $CoMn_2O_4$ for Toluene Oxidation: Involvement and Replenishment of Oxygen Species Using In Situ Designed-TP Techniques, ACS Catal. 9 (2019) 6698–6710.
[61] R.Z. Yarbay Şahin, M. Duplančić, V. Tomašić, J.H. Badia i Córcoles, S. Kurajica, Essential role of B metal species in perovskite type catalyst structure and activity on toluene oxidation, Inter. J. Environ. Sci. Technol. 19 (1) (2022) 553–564.
[62] S. Zhao, K. Li, S. Jiang, J. Li, pd-Co based spinel oxides derived from pd nanoparticles immobilized on layered double hydroxides for toluene combustion, Appl. Catal. B: Environ. 181 (2016) 236–248.
[63] C.H. Zhang, C. Wang, H. Huang, K. Zeng, Z. Wang, H.P. Jia, X.B. Li, Insights into the size and structural effects of zeolitic supports on gaseous toluene oxidation over MnO_x/HZSM-5 catalysts, Appl. Surf. Sci. 486 (2019) 108–120.
[64] Y. Zhang, J.C. Lu, L.M. Zhang, T. Fu, J. Zhang, X. Zhu, X.Y. Gao, D.D. He, Y.M. Luo, D.D. Dionysiou, W.J. Zhu, Investigation into the catalytic roles of oxygen vacancies during gaseous styrene degradation process via CeO_2 catalysts with four different morphologies, Appl. Catal. B: Environ. 309 (2022), 121249.
[65] L. Zhang, S.M. Zhu, R.Z. Li, W. Deng, C. Hong, D.Q. Liu, L.M. Guo, Ag-Doped delta-MnO_2 Nanosheets as Robust Catalysts for Toluene Combustion, ACS Appl. Nano Mater. 3 (2020) 11869–11880.
[66] L. Chen, W. Cui, J. Li, H. Wang, X. Dong, P. Chen, Y. Zhou, F. Dong, The high selectivity for benzoic acid formation on $ca_2Sb_2O_7$ enables efficient and stable toluene mineralization, Appl. Catal. B: Environ. 271 (2020) 118948.
[67] J. Zhong, Y. Zeng, D. Chen, S. Mo, M. Zhang, M. Fu, J. Wu, Z. Su, P. Chen, D. Ye, Toluene oxidation over Co3+-rich spinel Co3O4: Evaluation of chemical and by-product species identified by in situ DRIFTS combined with PTR-TOF-MS, J. Hazard. Mater. 386 (2020), 121957.
[68] Z. Chen, Y. Peng, J. Chen, C. Wang, H. Yin, H. Wang, C. You, J. Li, Performance and mechanism of photocatalytic toluene degradation and catalyst regeneration by Thermal/UV treatment, Environ. Sci. Tech. 54 (22) (2020) 14465–14473.
[69] Z. Xuejun, L. Haiyang, S. Zhongxian, L. Wei, L. Zepeng, M. Dujuan, G. Hongrun, Z. Mengru, In situ DRIFT spectroscopy study into the reaction mechanism of toluene over CeMo catalysts, J. Environ. Chem. Eng. 10 (2022), 108895.
[70] T. Gan, X.F. Chu, H. Qi, W.X. Zhang, Y.C. Zou, W.F. Yan, G. Liu, Pt/Al_2O_3 with ultralow Pt-loading catalyze toluene oxidation: Promotional synergistic effect of Pt nanoparticles and Al_2O_3 support, Appl. Catal. B: Environ. 257 (2019), 117943.
[71] Y.D. Zhang, C.T. Li, Y.C. Zhu, X.Y. Du, Y. Lyu, S.H. Li, Y.B. Zhai, Insight into the enhanced performance of toluene removal from simulated flue gas over Mn-Cu oxides modified activated coke, Fuel 276 (2020), 118099.
[72] X. Yang, X. Ma, X. Yu, M. Ge, Exploration of strong metal-support interaction in zirconia supported catalysts for toluene oxidation, Appl. Catal. B: Environ. 263 (2020), 118355.
[73] J. Zhong, Y. Zeng, M. Zhang, W. Feng, D. Xiao, J. Wu, P. Chen, M. Fu, D. Ye, Toluene oxidation process and proper mechanism over co_3O_4 nanotubes: Investigation through in situ DRIFTS combined with PTR-TOF-MS and quasi in-situ XPS, Chem. Eng. J. 397 (2020), 125375.
[74] E. Rezaei, J. Soltan, N. Chen, Catalytic oxidation of toluene by ozone over alumina supported manganese oxides: Effect of catalyst loading, Appl. Catal. B: Environ. 136 (2013) 239–247.
[75] Y. Zhu, C. Li, C. Liang, S. Li, X. Liu, X. Du, K. Yang, J. Zhao, Q. Yu, Y. Zhai, Y. Ma, Regulating CeO_2 morphologies on the catalytic oxidation of toluene at lower temperature: A study of the structure–activity relationship, J. Catal. 418 (2023) 151–162.